

to appear in *The Astrophysical Journal Letters* EVLA Special Issue

## First Results from a 1.3 cm EVLA Survey of Massive Protostellar Objects: G35.03+0.35

C. L. Brogan<sup>1</sup>, T. R. Hunter<sup>1</sup>, C. J. Cyganowski<sup>2,3</sup>,  
R. K. Friesen<sup>1</sup>, C. J. Chandler<sup>5</sup>, R. Indebetouw<sup>1,6</sup>

cbrogan@nrao.edu

### ABSTRACT

We have performed a 1.3 cm survey of 24 massive young stellar objects (MYSOs) using the Expanded Very Large Array (EVLA). The sources in the sample exhibit a broad range of massive star formation signposts including Infrared Dark Clouds (IRDCs), UCHII regions, and extended  $4.5\mu\text{m}$  emission in the form of Extended Green Objects (EGOs). In this work, we present results for G35.03+0.35 which exhibits all of these phenomena. We simultaneously image the 1.3 cm  $\text{NH}_3$  (1,1) through (6,6) inversion lines, four  $\text{CH}_3\text{OH}$  transitions, two H recombination lines, plus continuum at 0.05 pc resolution. We find three areas of thermal  $\text{NH}_3$  emission, two within the EGO (designated the NE and SW cores) and one toward an adjacent IRDC. The NE core contains an UCHII region (CM1) and a candidate HCHII region (CM2). A region of non-thermal, likely masing  $\text{NH}_3$  (3,3) and (6,6) emission is coincident with an arc of 44 GHz  $\text{CH}_3\text{OH}$  masers. We also detect two new 25 GHz Class I  $\text{CH}_3\text{OH}$  masers. A complementary Submillimeter Array 1.3 mm continuum image shows that the distribution of dust emission is similar to the lower-lying  $\text{NH}_3$  lines, all peaking to the NW of CM2, indicating the likely presence of an additional MYSO in this protocluster. By modeling the  $\text{NH}_3$  and 1.3 mm continuum data, we obtain gas temperatures of 20-220 K and masses of 20-130  $M_\odot$ . The diversity of continuum emission properties and gas temperatures suggest that objects in a range of evolutionary states exist concurrently in this protocluster.

---

<sup>1</sup>NRAO, 520 Edgemont Rd, Charlottesville, VA 22903

<sup>2</sup>Harvard-Smithsonian Center for Astrophysics, Cambridge, MA 02138

<sup>3</sup>NSF Astronomy and Astrophysics Postdoctoral Fellow

<sup>5</sup>NRAO, 1003 Lopezville Rd, Socorro, NM 87801

<sup>6</sup>University of Virginia, Charlottesville, VA 22903

*Subject headings:* stars: formation — stars: massive — ISM: individual objects (G35.03+0.35) — techniques: interferometric

## 1. Introduction

Massive star formation is a phenomenon of fundamental importance in astrophysics, yet it remains poorly understood. Massive protostars form in complex clusters and predominantly at distances greater than a kiloparsec making them challenging to study (Zinnecker and Yorke 2007). Unfortunately, the tools used to study low mass YSOs (primarily near-IR imaging) are largely inapplicable due to extreme dust obscuration even into the mid-IR. Radio and millimeter wavelengths penetrate the dust, and have revealed a wide variety of phenomena associated with MYSOs: CH<sub>3</sub>OH, H<sub>2</sub>O, and OH masers, hyper-compact (HC) and ultra-compact (UC) H II regions, recombination lines, infrared dark clouds (IRDCs), warm (> 30 K) dust cores, massive outflows, extended 4.5  $\mu$ m emission from shocks, and hot core line emission. However, these signposts have been compiled from a heterogeneous set of observations with varying angular resolution and sensitivity, making correlation analyses difficult.

In order to advance our understanding of MYSOs, we are using the EVLA to observe 24 MYSOs with  $\sim 10,000$  AU resolution in 1.3 cm continuum and a comprehensive set of diagnostic lines *simultaneously*. This resident shared risk observing project is among the first to utilize 16 spectral windows with high spectral resolution including: the NH<sub>3</sub> ladder from (1,1) to (6,6) ( $E_l=23$  - 540 K); four CH<sub>3</sub>OH transitions that can show maser emission; two H recombination lines; and other potential hot core species; plus reasonable continuum sensitivity. The majority (22/24) of our sample originates from the Cyganowski et al. (2008) catalog of MYSO outflow candidates (extended green objects, EGOs, selected based on extended 4.5 $\mu$ m emission). Many EGOs are located in IRDCs (for an overview of IRDCs see Rathborne et al. 2006), with a smaller subset associated with HC or UCHII regions. To explore the range in the properties of MYSOs associated with extended 4.5 $\mu$ m shock emission, the sample includes five EGOs with compact HII regions, as well as two non-EGOs for comparison (an IRDC and a UCHII region). In this paper, we present the first results from the survey by describing the observations of one source in detail: G35.03+0.35 (hereafter, G35.03). To show the location of dust emission with respect to the centimeter emission, we include complementary 1.3 mm Submillimeter Array (SMA) observations.

### 1.1. Background on G35.03+0.35

G35.03 is an EGO at a distance of  $\sim 3.4$  kpc with a bipolar  $4.5 \mu\text{m}$  morphology oriented NE-SW at a systemic velocity of  $\sim 53.1 \text{ km s}^{-1}$  based on  $\text{H}^{13}\text{CO}^+$  (3-2) single dish data (Cyganowski et al. 2009). A saturated *Spitzer* MIPS GAL 24  $\mu\text{m}$  source is located near the center of the two lobes and is coincident with five compact centimeter continuum sources called CM1...CM5 in order of decreasing flux (Cyganowski et al. 2011). CM1 has a flat centimeter spectral index ( $\alpha \sim -0.1$ ,  $S_\nu \propto \nu^\alpha$ ) consistent with optically thin free-free emission from an UC H II region (also see Kurtz et al. 1994; Argon et al. 2000). In contrast CM2 has a rising spectrum ( $\alpha \sim +0.7$ ), suggesting it may be a HC H II region or wind/jet source (Cyganowski et al. 2011). Coincident with CM2 are blueshifted Class-II 6.7 GHz  $\text{CH}_3\text{OH}$  masers ( $\Delta V \sim 6 - 12 \text{ km s}^{-1}$ ; Cyganowski et al. 2009), blueshifted OH masers ( $\Delta V \sim 3 - 14 \text{ km s}^{-1}$ ; Argon et al. 2000), and redshifted  $\text{H}_2\text{O}$  masers ( $\Delta V \sim 13 - 17 \text{ km s}^{-1}$ ; Forster and Caswell 1999). Additionally, an arc-like structure of outflow-tracing Class-I 44 GHz  $\text{CH}_3\text{OH}$  masers are located toward the Eastern side of the EGO (Cyganowski et al. 2009).

## 2. Observations

The NRAO<sup>1</sup> Expanded Very Large Array (EVLA) observations are summarized in Table 1; see Perley et al. (2011) for additional details on the EVLA system. The EVLA data were calibrated and imaged in CASA<sup>2</sup>. All images were restored with a synthesized beam of  $3''.7 \times 3''.0$  (P.A. =  $-50^\circ$ ), corresponding to  $\sim 12,600 \times 10,000$  AU at 3.4 kpc.

The SMA<sup>3</sup> observations are also summarized in Table 1. The sidebands were centered at 220.1 and 230.1 GHz. The data were calibrated in MIRIAD, then exported to CASA for self-calibration and imaging. In this paper we only consider the 1.3 mm continuum data estimated from line-free channels in the uv-plane. The SMA spectral line data will be described in a future publication.

---

<sup>1</sup>The National Radio Astronomy Observatory is a facility of the National Science Foundation operated under agreement by the Associated Universities, Inc.

<sup>2</sup><http://casa.nrao.edu/>

<sup>3</sup>The Submillimeter Array (SMA) is a collaborative project between the Smithsonian Astrophysical Observatory and the Academia Sinica Institute of Astronomy & Astrophysics of Taiwan.

### 3. Results

As shown in Figure 1a, we detect three major regions of  $\text{NH}_3$  (1,1) emission: (i) the strongest emission is coincident with the central region of the bipolar  $4.5 \mu\text{m}$  nebulosity, the five centimeter continuum sources described in §1.1, and 6.7 GHz  $\text{CH}_3\text{OH}$  masers; (ii) a slightly weaker and more compact core coincident with the SW lobe of the bipolar  $4.5 \mu\text{m}$  nebulosity; and (iii) a weak but extended core coincident with the IRDC  $\sim 30''$  SW of the EGO. Figures 1b and c show the intensity weighted velocity field and velocity dispersion of the  $\text{NH}_3$  (1,1) emission, respectively. The emission spans a velocity range of about  $4 \text{ km s}^{-1}$ , with a distinct NE-SW blue-red velocity gradient across the EGO. This velocity gradient is not clearly associated with an outflow, but instead seems to trace a shift in systemic velocity across the region. The mean systemic velocity toward the EGO and the “Dark” core to the SW is  $\sim 54 \text{ km s}^{-1}$ . In the vicinity of the “NE” core (and the centimeter sources), the velocity dispersion shows a marked increase from  $\sim 0.6 \text{ km s}^{-1}$  to values as high as  $\sim 1.9 \text{ km s}^{-1}$ . There are also “fingers” of weak  $\text{NH}_3$  emission evident around the periphery of the EGO – these fingers are not apparent in the integrated intensity map (Fig. 1a) because as demonstrated in Fig. 1c they have extremely narrow velocity dispersion ( $\sim 0.25 \text{ km s}^{-1}$ ).

Figure 2a shows a detailed comparison of the EVLA  $\text{NH}_3$  (1,1) integrated intensity, SMA 1.3 mm continuum, and the VLA 3.6 cm continuum (Cyganowski et al. 2011, CM1 and CM2 are also detected in the line free channels of the current EVLA data; albeit at lower angular resolution and sensitivity). Overall, there is strong agreement between the  $\text{NH}_3$  and 1.3 mm continuum emission. The strongest 1.3 mm emission arises from the NE core, coincident with CM1 and CM2. Though it is difficult to quantify the free-free vs. dust contributions at 1.3 mm due to the mismatch in the continuum resolution (and  $uv$ -coverage) between the SMA, VLA, and EVLA (not shown), it is clear that a significant fraction must be due to dust. The morphology of the  $\text{NH}_3$  (1,1) and (2,2) emission (see Fig. 2b), along with the 1.3 mm emission to the NW of CM2, suggests the presence of a third compact source in the NE core lacking in free-free emission. Millimeter continuum emission is also visible to the East-SE of the NE-core that partially coincides with the arc of 44 GHz  $\text{CH}_3\text{OH}$  masers, and mimics the morphology of the  $\text{NH}_3$  (1,1) integrated intensity. The SW  $\text{NH}_3$  core also has a 1.3 mm counterpart. The “Dark” ammonia core was not detected by the SMA, probably due to the smaller primary beam of these data.

Figure 2c gives a detailed comparison of the  $\text{NH}_3$  (1,1), (3,3), and (6,6) integrated intensities. Significant (3,3) emission is detected toward both the NE and SW core regions, though the strongest emission is compact and located East of the EGO, toward the SE terminus of the 44 GHz maser arc. Interestingly, this region shows only weak para- $\text{NH}_3$  emission suggesting a non-thermal origin for the (3,3) emission, though it appears to be connected

to CM2 through a weaker ridge of warm thermal  $\text{NH}_3$  emission. The (6,6) transition is also detected at the (3,3) peak, as well as toward the candidate HC H II region CM2.

We also detect strong, spatially-unresolved emission in the  $\text{CH}_3\text{OH}$   $5_2 - 5_1$  and  $8_2 - 8_1$  lines at two distinct positions (Fig. 3). Using an upper limit to the fitted size of the emission ( $1''.5 \times 0''.6$ ), their peak flux densities ( $187 \pm 2$  mJy beam $^{-1}$  and  $39 \pm 2$  mJy beam $^{-1}$ ) correspond to brightness temperatures ( $T_b$ ) exceeding 400 and 85 K for the stronger and weaker source, respectively. These high  $T_b$  compared to the energy levels above ground (57 and 105 K) strongly suggest that these transitions are masing (25 GHz  $\text{CH}_3\text{OH}$  masers have also been observed for example in IRAS16547-4247, Voronkov et al. 2006). Interestingly, the transition of peak maser intensity switches from  $5_2 - 5_1$  for the stronger maser spot, to  $8_2 - 8_1$  for the weaker maser spot. The positions and peak velocities are (J2000)  $18^{\text{h}}54^{\text{m}}01.043^{\text{s}}$  ( $\pm 0.002\text{s}$ ),  $+02^{\circ}01'16''.86$  ( $\pm 0''.02$ ) at  $52.8$  km s $^{-1}$ , and  $18^{\text{h}}54^{\text{m}}00.562^{\text{s}}$  ( $\pm 0.002\text{s}$ ),  $+02^{\circ}01'17''.67$  ( $\pm 0''.02$ ) at  $55.2$  km s $^{-1}$  for the strong and weak masers, respectively (see Fig. 2a,b,c).

No emission greater than  $5\sigma$  was detected for the  $\text{SO}_2$ ,  $\text{DC}_3\text{N}$ ,  $\text{HC}_5\text{N}$ , and  $\text{HC}_9\text{N}$  transitions. The  $\text{H}63\alpha$  and  $\text{H}64\alpha$  recombination lines were detected toward the CM1 UC H II region at a peak velocity of  $55.9$  km s $^{-1}$ . Following the method of Garay et al. (1986), we use the line-to-continuum intensity ratio of 0.46, the fitted FWHM linewidth of  $17.6$  km s $^{-1}$ , and the diameter of CM1 determined from the EVLA 1.3 cm continuum ( $1''.3$ ) to derive an electron temperature of 7900 K and density of  $1.3 \times 10^4$  cm $^{-3}$ .

### 3.1. $\text{NH}_3$ Temperatures

Over the last few decades considerable progress has been made in understanding the excitation of the  $\text{NH}_3$  molecule under astrophysical conditions (see e.g. Maret et al. 2009). For example in cold regions, analysis of the (1,1) and (2,2) transitions has evolved toward simultaneous least squares-fitting of the line profiles – freeing the analysis from previous failures wherever the intensity of (2,2) rivals (1,1) (e.g. Rosolowsky et al. 2008). However, this type of analysis typically assumes that the kinetic temperature is much less than the energy gap between levels (41.5 K) such that only the (1,1) and (2,2) rotational levels are populated. Due to these assumptions, this technique becomes less accurate above temperatures of about 30 K. Generic molecular modeling packages exist that can be used to model  $\text{NH}_3$  emission from higher lying transitions using either radiative transfer with collisional excitation, or assuming LTE. However, no package currently combines separate ortho and para collision rates (with realistic collision partners) with the detailed hyperfine structure of  $\text{NH}_3$  and a partition function that includes all relevant states that may be excited in warm gas (though we can expect this situation to improve in the near future).

For the current preliminary analysis we have pursued the following course: (1) in the colder regions of G35.03 we have fit simultaneously the full hyperfine structure of the (1,1) and (2,2) lines using a non-linear, least squares Gaussian fitting routine given a single common line-of-sight-velocity, line width, excitation, and kinetic temperatures in IDL (Friesen et al. 2009); (2) In the warmer, and coincidentally more kinematically complex regions we have used the LTE method in the CASSIS<sup>4</sup> package to model all six observed NH<sub>3</sub> transitions, including multiple velocity components where necessary. To compare methods, we also fit the cooler regions with CASSIS. Figure 3a shows the results from technique (1), with grey areas indicating where this method’s assumptions are invalid. The fitted parameters for both techniques toward several representative positions are given in Table 2. The corresponding spectral line fits for these positions using technique (2) are shown in Figure 3d-h.

As shown in Table 2, the temperatures in the kinematically-simple Dark and SW core regions are in the 20-30 K range, with the latter being somewhat warmer on average. Both methods do a reasonable job here, with method (2) predicting about twice the total column density of (1), likely due to its more complete partition function. Toward the center of the NE core and along the 44 GHz maser arc, technique (1) breaks down for two reasons: (i) the gas is warm ( $\gtrsim 30$  K) throughout this region (or even non-thermal; Fig. 3b) and (ii) the lines become more kinematically complex with at least two distinct velocity components separated by about  $1.7 \text{ km s}^{-1}$ , or in the case of CM2 what appears to be a significantly blueshifted hot (220 K) outflow component. Towards CM1, the redder velocity component shows temperatures as high as  $\sim 70$  K.

### 3.2. Dust Mass

The average column densities and masses of the NE and SW cores based on the methodology described in Brogan et al. (2009, in Eqs. 4 and 5) using the 1.3 mm SMA data are shown in Table 2. The integrated 1.3 mm flux densities of the NE and SW cores are 831 and 170 mJy with estimated sizes of  $11.0''$  and  $6.8''$ , respectively. For the NE core, we have subtracted 25 mJy to account for the 3.6 cm flux of CM1 and CM2 (see Fig.2) assuming they are due entirely to free-free emission and using the 1.3 cm to 3.6 cm spectral indices derived by Cyganowski et al. (2011). For the range of temperatures derived from the NH<sub>3</sub> fits described in §3.1, the NE and SW cores have dust-based gas masses in the  $50 - 132 M_{\odot}$  and  $22 - 45 M_{\odot}$  range, respectively, and average column densities of  $(3 - 7) \times 10^{22} \text{ cm}^{-2}$ .

---

<sup>4</sup>CASSIS has been developed by CESR-UPS/CNRS (<http://cassis.cesr.fr>).

For comparison, Hill et al. (2005) report a SEST SIMBA 1.2 mm based mass for the whole G35.03 region of  $390 M_{\odot}$  assuming a dust temperature of 20 K and a total size of  $55''$  (includes the “Dark core” in addition to the NE and SW cores). The Bolocam Galactic Plane Survey (BGPS) catalog<sup>5</sup> reports a 1.1 mm flux of 1380 and 3030 mJy for G35.03 within  $40''$  and  $80''$  apertures, respectively (Rosolowsky et al. 2010). Assuming  $T_{dust} = 30$  K for  $r < 20''$  and  $T_{dust} = 20$  K for  $20'' < r < 40''$ , we find a total mass for the region of  $350 M_{\odot}$  ( $550 M_{\odot}$  if we multiply by the BGPS “correction factor” of 1.5), in reasonable agreement with Hill et al. (2005) and our SMA results, accounting for both the smaller primary beam and spatial filtering of the interferometer.

## 4. Discussion

### 4.1. Protocluster Nature of G35.03+0.35

Our high angular resolution observations reveal the presence of at least three MYSOs (possibly four if CM3 is included) within 20,000 AU of one another in the NE core (CM1, CM2, and NWCM2). This configuration suggests a Trapezium-like protocluster of massive stars like those identified in other similar regions (e.g. Hunter et al. 2006; Rodón et al. 2008). Component CM1 is a modest UC H II region associated with warm  $\text{NH}_3$  and hosts two velocity components which may indicate further unresolved structure. CM2 appears to be a HCH II region or wind/jet source exciting OH,  $\text{H}_2\text{O}$ , and Class II  $\text{CH}_3\text{OH}$  masers, and a hot (220 K) blueshifted outflow. The millimeter continuum source NW of CM2 exhibits the peak dust emission, no centimeter continuum emission, but the broadest Gaussian (non-outflow)  $\text{NH}_3$  profiles. Such diversity among the continuum properties and in the molecular gas temperatures toward these different objects is an increasingly familiar pattern seen in protoclusters (Zhang et al. 2007; Brogan et al. 2007). Similar to NGC6334I(N) (Brogan et al. 2009), the systemic velocities of these objects differ by up to  $1.7 \text{ km s}^{-1}$ , providing a measure of the cluster dynamics. However, detailed study of the kinematics requires higher angular resolution followup observations, in particular to spatially resolve the multiple velocity components toward the NE core objects.

---

<sup>5</sup>BGPS: [http://irsa.ipac.caltech.edu/data/BOLOCAM\\_GPS/](http://irsa.ipac.caltech.edu/data/BOLOCAM_GPS/)

## 4.2. New Masers in G35.03+0.35

As Figs. 2c, and 3b demonstrate, the (3,3) and (6,6)  $\text{NH}_3$  emission toward the terminus of the 44 GHz  $\text{CH}_3\text{OH}$  maser arc shows significant departure from LTE. Unfortunately, our current angular resolution precludes the measurement of the high brightness temperatures required for absolute confirmation of maser emission. Walmsley and Ungerechts (1983) first predicted that the (3,3) transition could undergo weak population inversion for densities of  $n \sim 10^{4-5} \text{ cm}^{-3}$  and temperatures of  $\sim 50 \text{ K}$  – physical conditions common in massive molecular outflows and similar to the conditions required to excite 44 GHz  $\text{CH}_3\text{OH}$  masers (Voronkov et al. 2005). We speculate that the non-thermal  $\text{NH}_3$  emission traces a bow shock from an outflow originating from CM2. Indeed, (3,3) maser emission has been detected previously in several regions of massive star formation mostly associated with strong outflows (e.g. DR 21(OH), NGC 6334I, IRAS20126+4104, G5.89-0.39 Mangum and Wootten 1994; Kraemer and Jackson 1995; Zhang et al. 1999; Hunter et al. 2008).

The stronger 25 GHz  $\text{CH}_3\text{OH}$  maser spot (Fig. 3c) is coincident in position and velocity with one of the weaker 44 GHz Class I masers from Cyganowski et al. (2009), and is within  $1.3''$  of the strongest 44 GHz maser. The weaker 25 GHz maser spot is located towards the SE edge of the CM1 UCHII region. Class I  $\text{CH}_3\text{OH}$  masers are thought to be excited by collisions in shocks, with the shock liberating methanol from dust grains and thus providing the necessary high column density. Sobolev et al. (2005) suggest that 25 GHz Class I masers require densities of  $\sim 10^{5-7} \text{ cm}^{-3}$  and temperatures of 75-100 K, hotter and denser than that required for 44 GHz class I masers. As demonstrated by Voronkov et al. (2006) detailed modeling of the ratio of brightness temperatures among the 25 GHz masing transitions can help to pinpoint the physical conditions. We hope to carry out such analysis for the ensemble of 25 GHz masers observed across our survey in the future.

## 5. Summary

We present the first results from a 1.3 cm survey of MYSOs using the EVLA, focusing on the EGO source G35.03+0.35. The new EVLA correlator allows us to simultaneously observe the  $\text{NH}_3$  (1,1) to (6,6) transitions, four  $\text{CH}_3\text{OH}$  transitions, two H recombination lines, and continuum. We find three major regions of dense  $\text{NH}_3$  gas, two (the NE and SW cores) being coincident with the EGO, and the third located in the adjacent IRDC. Using complementary SMA 1.3 mm and VLA 3.6 cm continuum data, along with temperatures derived from the  $\text{NH}_3$  emission, we find warm gas temperatures in the range 20-220 K, core masses in the 20-130  $M_\odot$  range, and average  $\text{H}_2$  column densities of several  $\times 10^{22} \text{ cm}^{-2}$ . Together these data reveal a massive protocluster in an early stage of formation with



members representing different phases of MYSO evolution concurrently. This work highlights the potential diagnostic power that the full survey will provide toward understanding the formation of massive stars and protoclusters.

Based on analysis using the CDMS, JPL, and Splatalogue spectroscopic databases, NASA’s Astrophysics Data System Bibliographic Services, and the SIMBAD database.

## REFERENCES

- Argon, A. L., Reid, M. J., & Menten, K. M. 2000, *ApJS*, 129, 159
- Brogan, C. L., Chandler, C. J., Hunter, T. R., Shirley, Y. L., & Sarma, A. P. 2007, *ApJ*, 660, L133
- Brogan, C. L., Hunter, T. R., Cyganowski, C. J., Indebetouw, R., Beuther, H., Menten, K. M., & Thorwirth, S. 2009, *ApJ*, 707, 1
- Cyganowski, C. J., Brogan, C. L., Hunter, T. R., and Churchwell, E.: 2011, *ApJ* 00
- Cyganowski, C. J., Brogan, C. L., Hunter, T. R., and Churchwell, E.: 2009, *ApJ* **702**, 1615
- Cyganowski, C. J., et al. 2008, *AJ* **136**, 2391
- Forster, J. R. and Caswell, J. L.: 1999, *A&AS* **137**, 43
- Friesen, R. K., Di Francesco, J., Shirley, Y. L., & Myers, P. C. 2009, *ApJ*, 697, 1457
- Garay, G., Rodriguez, L. F., and van Gorkom, J. H.: 1986, *ApJ* **309**, 553
- Hill, T., Burton, M. G., Minier, V., Thompson, M. A., Walsh, A. J., Hunt-Cunningham, M., & Garay, G. 2005, *MNRAS*, 363, 405
- Hunter, T. R., Brogan, C. L., Indebetouw, R., and Cyganowski, C. J.: 2008, *ApJ* **680**, 1271
- Hunter, T. R., Brogan, C. L., Megeath, S. T., Menten, K. M., Beuther, H., & Thorwirth, S. 2006, *ApJ*, 649, 888
- Kraemer, K. E. and Jackson, J. M.: 1995, *ApJ* **439**, L9
- Kurtz, S., Churchwell, E., and Wood, D. O. S.: 1994, *ApJS* **91**, 659
- Mangum, J. G. and Wootten, A.: 1994, *ApJ* **428**, L33

- Maret, S., Faure, A., Scifoni, E., & Wiesenfeld, L. 2009, *MNRAS*, 399, 425
- Perley, R.A., Chandler, C.J., Butler, B.J., Wrobel, J.M. 2011, *ApJ*, in press
- Rathborne, J. M., Jackson, J. M., and Simon, R.: 2006, *ApJ* **641**, 389
- Rodón, J. A., Beuther, H., Megeath, S. T., & van der Tak, F. F. S. 2008, *A&A*, 490, 213
- Rosolowsky, E. W., Pineda, J. E., Foster, J. B., Borkin, M. A., Kauffmann, J., Caselli, P., Myers, P. C., & Goodman, A. A. 2008, *ApJS*, 175, 509
- Rosolowsky, E., et al. 2010, *ApJS* **188**, 123
- Sobolev, A. M., Ostrovskii, A. B., Kirsanova, M. S., Shelemei, O. V., Voronkov, M. A., and Malyshev, A. V.: 2005, in R. Cesaroni, M. Felli, E. Churchwell, & M. Walmsley (ed.), *Massive Star Birth: A Crossroads of Astrophysics*, Vol. 227 of *IAU Symposium*, pp 174–179
- Voronkov, M., Sobolev, A., Ellingsen, S., Ostrovskii, A., & Alakoz, A. 2005, *Ap&SS*, 295, 217
- Voronkov, M. A., Brooks, K. J., Sobolev, A. M., Ellingsen, S. P., Ostrovskii, A. B., and Caswell, J. L.: 2006, *MNRAS* **373**, 411
- Walmsley, C. M. and Ungerechts, H.: 1983, *A&A* **122**, 164
- Zhang, Q., et al. 2007, *ApJ*, 658, 1152
- Zhang, Q., Hunter, T. R., Sridharan, T. K., & Cesaroni, R. 1999, *ApJ*, 527, L117
- Zinnecker, H. and Yorke, H. W.: 2007, *ARA&A* **45**, 481

Table 1. Observing parameters

Parameter	Value
EVLA 1.3 cm ( $\sim 24$ GHz) AB1346 observations	
Observing date (duration)	07 Sep 2010 (3 hours)
Configuration	D
Primary beamsize	2'
Bandwidth	16 $\times$ 8 MHz, single polarization
Baseband 0 subbands (MHz), <sup>a</sup> lines	23692.78, NH <sub>3</sub> (1,1) 23724.78, NH <sub>3</sub> (2,2) 23828.78, OH <sup>2</sup> $\Pi_{9/2}$ (5 <sup>-</sup> – 5 <sup>+</sup> ) 23868.78, NH <sub>3</sub> (3,3) 24084.78, SO <sub>2</sub> (8 <sub>2,6</sub> – 9 <sub>1,9</sub> ) 24140.78, NH <sub>3</sub> (4,4) 24508.78, H64 $\alpha$ 24532.78, NH <sub>3</sub> (5,5)
Baseband 1 subbands (MHz), <sup>a</sup> lines	24927.88, CH <sub>3</sub> OH (3 <sub>2,1</sub> – 3 <sub>1,2</sub> ) 24959.88, CH <sub>3</sub> OH (5 <sub>2,3</sub> – 5 <sub>1,4</sub> ) 25023.88, NH <sub>2</sub> D (4 <sub>1,4</sub> – 4 <sub>0,4</sub> ) 25055.88, NH <sub>3</sub> (6,6) 25295.88, CH <sub>3</sub> OH (8 <sub>2,6</sub> – 8 <sub>1,7</sub> ) 25327.88, DC <sub>3</sub> N (3-2) 25687.88, H63 $\alpha$ 25979.88, CH <sub>3</sub> OH (10 <sub>2,8</sub> – 10 <sub>1,9</sub> )
Velocity resolution	0.4 km s <sup>-1</sup>
Angular resolution <sup>b</sup>	3".7 $\times$ 3".0 (P.A.= $-50^\circ$ )
Spectral line rms noise <sup>c</sup>	3 mJy beam <sup>-1</sup> channel <sup>-1</sup>
Gain calibrator	J1815+0035
Bandpass and Flux Calibrator <sup>d</sup>	J1924-2914 (17.1 Jy assumed)

Table 1—Continued

Parameter	Value
SMA 1.3 mm ( $\sim$ 225 GHz) observations	
Observing date (duration)	24 Jun 2008 (11 hours)
Configuration	compact-north
Primary beamsize	52''
Bandwidth	2 $\times$ 2 GHz, single polarization
Velocity resolution	1.1 km s <sup>-1</sup>
Angular resolution <sup>b</sup>	3''.2 $\times$ 1''.8 (P.A.=+70°)
Continuum rms noise	3 mJy beam <sup>-1</sup>
Gain Calibrators	J1733-130 & J1751+096
Bandpass Calibrator	3C454.3
Flux Calibrator	Uranus

<sup>a</sup>These are the rest frame subband center frequencies; because the subbands were required to be on an 8 MHz grid, the lines are offset from the centers. Line rest frequencies were obtained from <http://splatalogue.net>.

<sup>b</sup>Briggs weighting of 0.5.

<sup>c</sup>Due to its inadvertent proximity to a subband filter edge, the NH<sub>3</sub> (2,2) subband is a factor of two noisier than the others.

<sup>d</sup><sup>3</sup>C 286 observation failed, used bootstrapped flux density of J1924-2914 from previous track.

Table 2. Fitted Parameters

Source <sup>a</sup>	Single Gaussian 2-level NH <sub>3</sub> Fits				Full Multitransition CASSIS NH <sub>3</sub> Fits				Estimates from 1.3 mm Continuum		
	$V_{LSR}$ (km s <sup>-1</sup> )	$\Delta V_{FWHM}$ (km s <sup>-1</sup> )	$T_k$ (K)	$N_{NH_3}$ ( $\times 10^{15}$ cm <sup>-2</sup> )	$V_{LSR}$ (km s <sup>-1</sup> )	$\Delta V_{FWHM}$ (km s <sup>-1</sup> )	$T_k$ (K)	$N_{NH_3}$ ( $\times 10^{15}$ cm <sup>-2</sup> )	$T_{dust}$ (K)	$M_{gas}$ (M <sub>⊙</sub> )	$N_{H_2}$ ( $\times 10^{22}$ cm <sup>-2</sup> )
NE Core	...	...	...	...	...	...	...	...	70 - 30	50 - 132	3 - 7
CM1-v1	...	...	...	...	53.7	1.3	40	2.0	...	...	...
CM1-v2	...	...	...	...	55.4	1.3	70	3.2	...	...	...
CM2-v1	...	...	...	...	53.8	1.8	30	3.5	...	...	...
CM2-v2	...	...	...	...	50.0	3.0	35	2.0	...	...	...
CM2-v3	...	...	...	...	49.2	3.0	220	2.0	...	...	...
NW CM2	53.3	2.8	41	2.1	53.8	2.2	33	6.0	...	...	...
SW Core	54.7	1.1	25	3.0	54.9	1.2	27	5.5	35 - 20	22 - 45	3 - 6
Dark Core	53.9	1.0	20	1.2	54.2	1.1	18	2.6	...	...	...

<sup>a</sup>Positions for these fits are (J2000): CM1: 18<sup>h</sup>54<sup>m</sup>00.488<sup>s</sup>, +02°01′18″21; CM2: 18<sup>h</sup>54<sup>m</sup>00.650<sup>s</sup>, +02°01′19″05; NW CM2: 18<sup>h</sup>54<sup>m</sup>00.561<sup>s</sup>, +02°01′21″72; SW core: 18<sup>h</sup>54<sup>m</sup>00.164<sup>s</sup>, +02°01′11″78; Dark Core: 18<sup>h</sup>53<sup>m</sup>59.396<sup>s</sup>, +02°01′01″47.

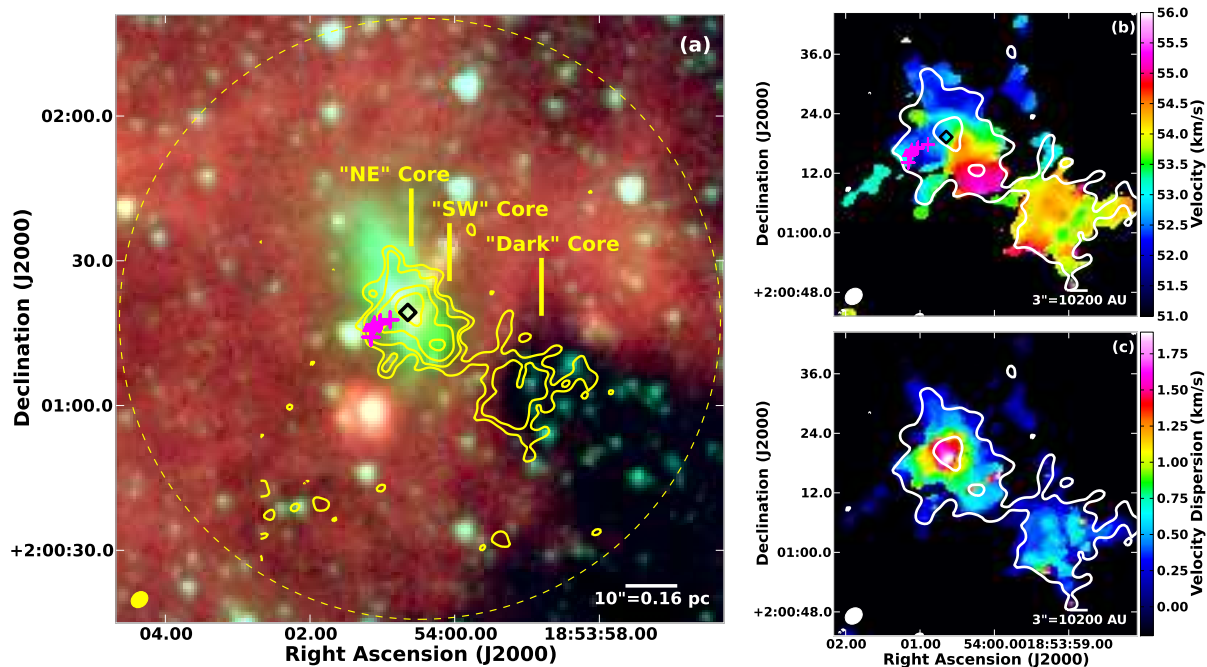


Fig. 1.— (a) *Spitzer* GLIMPSE three-color image of EGO G35.03 with RGB mapped to 8.0, 4.5, and 3.6  $\mu\text{m}$  overlaid with the EVLA primary beam (yellow dashed circle). Yellow contours show the  $\text{NH}_3$  (1,1) integrated intensity (contours at 16, 28, 56, and 102  $\text{mJy beam}^{-1} \cdot \text{km s}^{-1}$ ). The three brightest  $\text{NH}_3$  cores are labeled for reference. Magenta + symbols and a single black  $\diamond$  mark the locations of the 44 and 6.7 GHz  $\text{CH}_3\text{OH}$  masers from Cyganowski et al. (2009). (b) and (c) show the  $\text{NH}_3$  (1,1) velocity field (moment 1) and velocity dispersion (moment 2) with the lowest and highest (1,1) integrated intensity contour levels from (a) superposed in white. In all three panels, the EVLA synthesized beam is shown in the lower left.

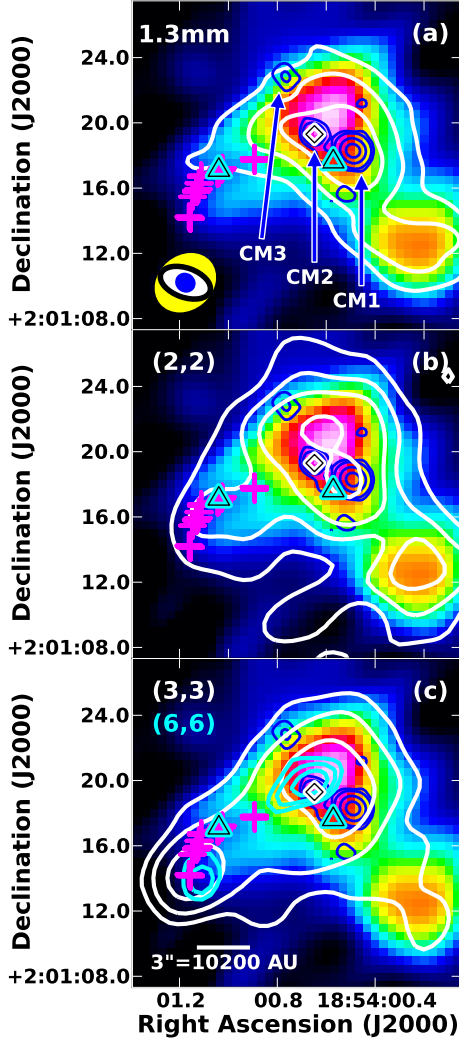


Fig. 2.— Zoomed-in view of the NE and SW cores showing the  $\text{NH}_3$  (1,1) integrated intensity in colorscale with VLA 3.6 cm continuum contours (0.1, 0.3, 2, 7  $\text{mJy beam}^{-1}$ ) from Cyganowski et al. (2011) superposed in blue; the three brightest centimeter continuum sources are labeled CM1, CM2, and CM3. (a) SMA 1.3 mm continuum is shown in white contours (levels: 7, 30, and 90  $\text{mJy beam}^{-1}$ ) and the synthesized beams of the EVLA (yellow), VLA (blue), and SMA (white) are shown in the lower left corner. (b) White contours show the integrated intensity of  $\text{NH}_3$  (2,2) (levels: 25, 50, 75, and 117  $\text{mJy beam}^{-1} \cdot \text{km s}^{-1}$ ). (c) Contours show the integrated intensity of  $\text{NH}_3$  (3,3) (white; 30, 60, and 120  $\text{mJy beam}^{-1} \cdot \text{km s}^{-1}$ ) and (6,6) (cyan; 13, 17, and 22  $\text{mJy beam}^{-1} \cdot \text{km s}^{-1}$ ). In all panels, the locations of two new 25 GHz  $\text{CH}_3\text{OH}$  masers are cyan triangles, and the 6.7 and 44 GHz  $\text{CH}_3\text{OH}$  masers from Fig 1 are also shown.

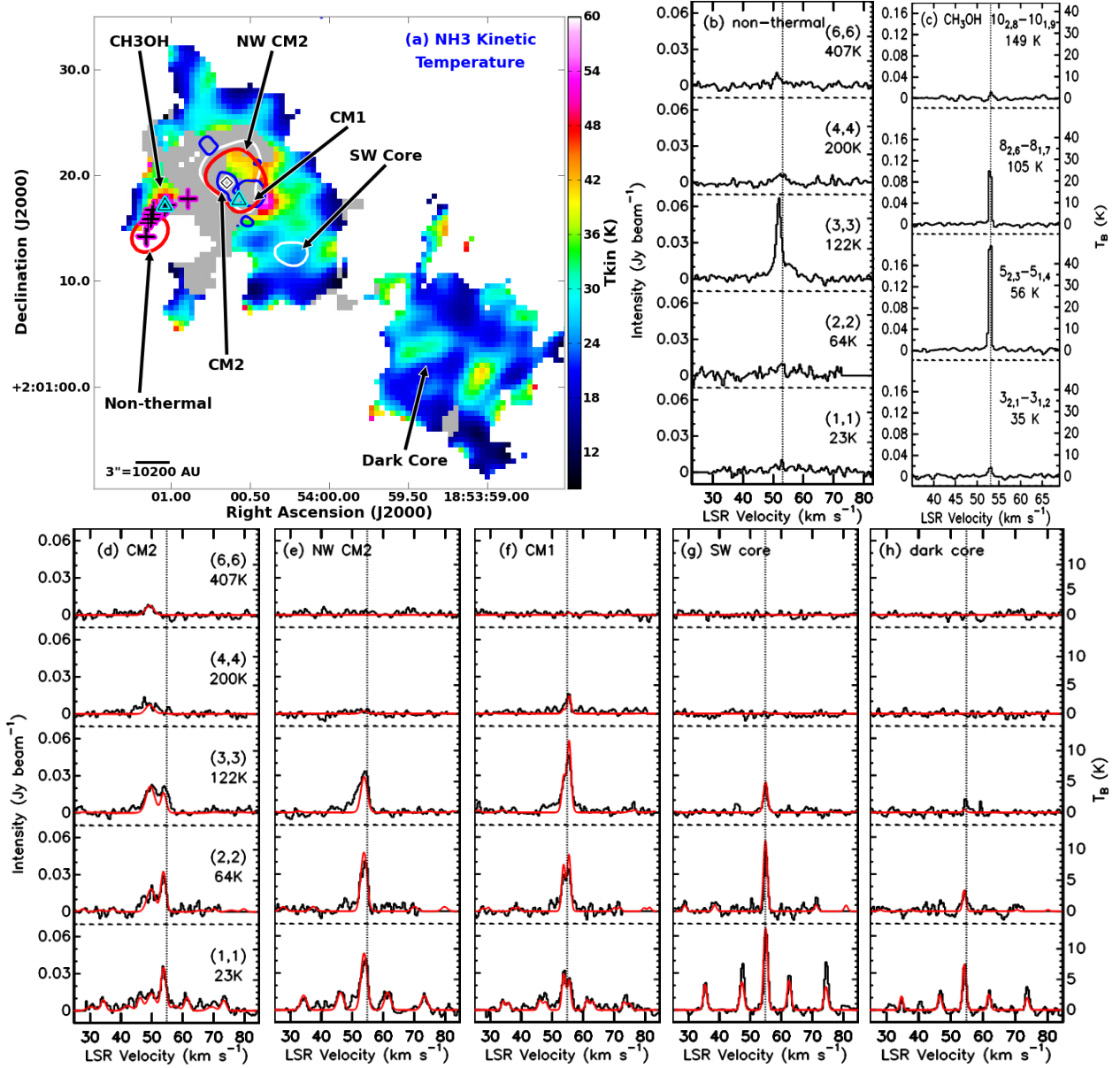


Fig. 3.— (a) Colorscale of the NH<sub>3</sub> kinetic temperature derived from single Gaussian two-level fits; grey areas indicate where the assumptions for this technique are invalid. The blue, red, and white contours show the lowest 3.6 cm contour from Fig. 2, highest (3,3) contour from Fig. 2c, and highest (1,1) contour from Fig. 1a, respectively. The locations of the profiles shown in (b), for the non-thermal NH<sub>3</sub> emission (18<sup>h</sup>54<sup>m</sup>01.119<sup>s</sup>, +02°01′14″.08) and (c) the stronger 25 GHz CH<sub>3</sub>OH maser (18<sup>h</sup>54<sup>m</sup>01.076<sup>s</sup>, +02°01′16″.47) are indicated along with other positions fitted with method (2) and presented in Table 2. On (b) and (c), the vertical dotted line marks the LSR velocity of +53.1 km s<sup>-1</sup>. (d)-(h) Observed NH<sub>3</sub> spectra (black) overlaid with fitted profiles (red) using full LTE modeling in CASSIS (see Table 2).